



A STUDY OF RO-VIBRATIONAL OH EMISSION FROM HERBIG Ae/Be STARS

SEAN D. BRITTAIN¹, JOAN R. NAJITA², JOHN S. CARR³, MÁTÉ ÁDÁMKOVICS⁴, AND NICKALAS REYNOLDS¹

¹ Department of Physics & Astronomy, 118 Kinar Laboratory, Clemson University, Clemson, SC 29634-0978, USA; sbritt@clemson.edu

² National Optical Astronomy Observatory, 950 N. Cherry Ave., Tucson, AZ 85719, USA

³ Naval Research Laboratory, Code 7211, Washington, DC 20375, USA

⁴ Department of Astronomy, University of California, Berkeley, CA 94720-3411, USA

Received 2016 March 16; revised 2016 July 22; accepted 2016 July 27; published 2016 October 17

ABSTRACT

We present a study of ro-vibrational OH and CO emission from 21 disks around Herbig Ae/Be stars. We find that the OH and CO luminosities are proportional over a wide range of stellar ultraviolet luminosities. The OH and CO line profiles are also similar, indicating that they arise from roughly the same radial region of the disk. The CO and OH emission are both correlated with the far-ultraviolet luminosity of the stars, while the polycyclic aromatic hydrocarbon (PAH) luminosity is correlated with the longer wavelength ultraviolet luminosity of the stars. Although disk flaring affects the PAH luminosity, it is not a factor in the luminosity of the OH and CO emission. These properties are consistent with models of UV-irradiated disk atmospheres. We also find that the transition disks in our sample, which have large optically thin inner regions, have lower OH and CO luminosities than non-transition disk sources with similar ultraviolet luminosities. This result, while tentative given the small sample size, is consistent with the interpretation that transition disks lack a gaseous disk close to the star.

Key words: circumstellar matter – line: profiles – molecular processes – protoplanetary disks

1. INTRODUCTION

Herbig AeBe stars (HAeBes) are young ($\lesssim 10$ Myr) intermediate-mass ($2\text{--}8 M_{\odot}$) stars whose spectral energy distribution (SED) reveals an infrared (IR) excess (Herbig 1960; Waters & Waelkens 1998; Vieira et al. 2003). They are the precursors to main sequence A-stars, many of which have debris disks (Su et al. 2005, 2006) and planets, e.g., as evidenced by planets around “retired” A-stars (Johnson et al. 2010); the pollution of white dwarfs (Zuckerman et al. 2010); and direct imaging of companions (Lagrange et al. 2009).

HAeBes are characterized as either Group I (flared disks) or Group II (self-shadowed disks) sources based on the IR color of the SED (Meeus et al. 2001; Dullemond & Monnier 2010). It has been suggested that Group I HAeBes have disks with gaps (i.e., transitional disks; Honda et al. 2012; Maaskant et al. 2013). If so, and if these gaps are formed by giant planets, this would confirm the inference that gas giant planets are common around more massive stars (Johnson et al. 2010). Thus HAeBes are prime candidates for studying the signatures of forming supra-Jovian mass companions.

Ro-vibrational emission lines from diatomic molecules such as CO and OH are valuable diagnostics of the inner, planet-forming region of disks around young stars. The properties of ro-vibrational CO emission from disks surrounding HAeBes have been studied extensively (e.g., Blake & Boogert 2004; Brittain et al. 2007; Banzatti & Pontoppidan 2015; van der Plas et al. 2015). However, ro-vibrational OH emission has only been observed in a few HAeBes (Mandell et al. 2008; Fedele et al. 2011; Liskowsky et al. 2012). The observation of OH emission is challenging due to the weakness of the features (typically $\lesssim 1\%$ – 3% of the continuum). This is in part because the fundamental ro-vibrational transitions of OH are divided over four times as many lines as the fundamental ro-vibrational transitions of CO. The total angular momentum of the ground electronic state is $\Lambda = 1$ so that it is doubly degenerate and each rotational level within the ground electronic state is split

(Λ -doubling). Thus, for similar temperatures and abundances, one would expect the fundamental ro-vibrational OH emission lines to be about a factor of four weaker than the fundamental ro-vibrational CO emission lines. However, there has not been a systematic study of how the OH and CO emissions from HAeBes compare. The goal of this study is to characterize the OH emission from a group of HAeBes spanning a wide range of spectral types and disk geometries to better understand its relation to the more familiar CO emission as well as what determines the abundance and excitation of OH.

Here we present a study of ro-vibrational OH emission from 21 HAeBes. We focus on the ${}^2\Pi_{3/2}$ P4.5(1+, 1−) doublet to facilitate comparison with previous studies (e.g., Mandell et al. 2008; Fedele et al. 2011) and because this is the transition with the lowest upper level energy state regularly accessible from the ground. At 3860 cm^{-1} above the ground state, the energy of the upper level of this transition is comparable to that of the $\nu = 1\text{--}0$ P19 CO line ($E' = 3880\text{ cm}^{-1}$). The spectra analyzed in this paper were culled from previous observations in the literature (Mandell et al. 2008; Fedele et al. 2011; Liskowsky et al. 2012), data taken from the archives, and new observations. The sample is roughly evenly divided between Group I and Group II sources spanning a broad range of spectral types. To look at the roles various thermo-chemical process play in the excitation of OH emission in disks around HAeBes, we explore the relationship between the luminosity of OH emission and the disk geometry, ultraviolet luminosity of the star, the luminosity of polycyclic aromatic hydrocarbon (PAH) emission, and ro-vibrational CO emission.

2. OBSERVATIONS

We present new observations of eight HAeBes in the L -band and six HAeBes in the M -band (Table 1). Seven of the L -band observations were obtained at the W. M. Keck Observatory with the NIRSPEC echelle spectrograph (McLean et al. 1998). This instrument provided a resolving power of $\lambda/\Delta\lambda = 25,000$. One source, HD 142527, was observed with

Table 1
Log of Observations

Star	Date Obs	Airmass	Int Time m
<i>L</i> -band data			
HD 179218	2014 Sep 13	1.02	48
V380 Ori	2014 Sep 13	1.46	44
HD 135344b	2009 Jul 13	1.84	16
LkH α 224	2014 Sep 13	1.09	56
HD 142527	2013 May 29	1.05	10
Elias 3-1	2014 Sep 13	1.24	76
HD 141569	2014 Apr 8	1.16	32
HD 190073	2014 Sep 13	1.31	40
<i>M</i> -band data			
V380 Ori	2006 Jan 13	1.65	16
CO Ori	2006 Jan 13	1.91	20
HD 34282	2006 Jan 14	1.07	40

CRILES on the European Southern Observatory Very Large Telescope (Käufl et al. 2004). Our team collected the data for six of the sources. HD 135344b was taken from the Keck Observatory Archive and HD 142527 was taken from the ESO Archive. Among the *M*-band observations, three sources (V380 Ori, HD 34282, and CO Ori) were obtained at Gemini South Observatory with the PHOENIX echelle spectrograph (Hinkle et al. 1998, 2000, 2003). This instrument provided a resolving power of $\lambda/\Delta\lambda = 50,000$. Three other sources were taken from the Keck Observatory Archive (HD 36112, UX Ori, and BF Ori).

Even at the “blue” end of the *L*-band where the $v = 1 - 0$ P4.5(1+, 1-) OH doublet falls, there is a significant thermal continuum background upon which are superimposed night sky emission lines (mostly water). The intensities of these telluric lines scale with the air mass and column density of atmospheric water vapor, which can vary both temporally and spatially through the night. To cancel the sky emission, the telescope was nodded $15''$, along the slit axis in an A, B, B, A sequence with each step corresponding to one minute of integration time. Combining the scans as $(A-B-B+A)/2$ canceled the background to first order.

Flats and darks were taken before the grating was moved and used to remove systematic effects. The two-dimensional frames were cleaned of systematically hot and dead pixels as well as cosmic ray hits, and were then resampled spatially and spectrally so that the spectral and spatial dimensions were orthogonal. The CRILES spectrum was reduced using the ESO CRILES pipeline following a similar procedure.

The data were wavelength calibrated by fitting the telluric lines in the spectra with the Spectrum Synthesis Program (SSP Kunde & Maguire 1974), which accesses the 2000 HITRAN molecular database (Rothman et al. 2003). Spectra of hot stars were taken at similar airmasses throughout the observations for telluric correction. The line fluxes were calculated by scaling the equivalent width to the continuum flux inferred from ground-based IR photometry. The log of the observations is presented in Table 1 and the telluric corrected spectra are presented in Figure 1.

Our full sample of HAeBes have spectral types that range from F7 to B2 (Table 2). In addition to the new observations presented here, we include 13 previously published OH measurements (Mandell et al. 2008; Fedele et al. 2011; Brittain et al. 2014) and 9 previously published CO measurements

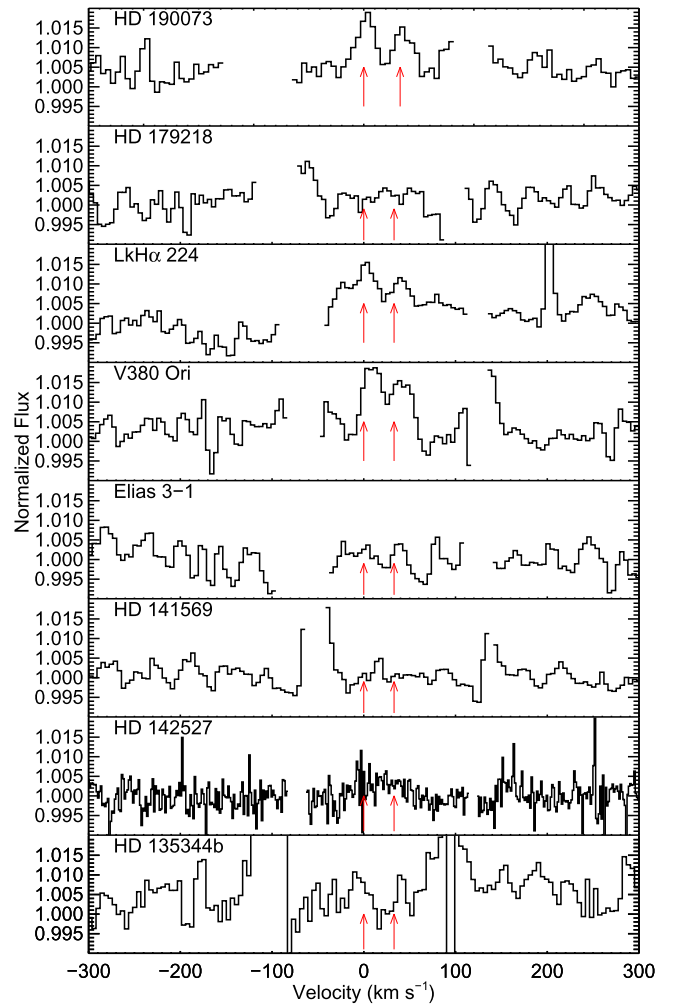


Figure 1. Spectra covering the location of the OH $v = 1-0$ P4.5 doublet. OH emission is detected in HD 190073, Lk H α 224, V380 Ori, and HD 142527. The spectra are plotted in the rest-frame of the star and the expected location of the OH doublet is marked with a pair of red arrows.

(Brittain et al. 2007; van der Plas et al. 2015) of HAeBes (Table 3).

3. RESULTS

The $v = 1-0$ ${}^2\Pi_{3/2}$ P4.5(1+, 1-) OH emission doublet is detected in four of the eight sources reported in this paper (Figure 1). This is consistent with the overall detection rate of OH reported in the literature (6 of 13; Table 3; Mandell et al. 2008; Fedele et al. 2011; Liskowsky et al. 2012).

HAeBes are broadly separated into two groups: those with flaring disks (Group I) and those with flat disks (Group II; Meeus et al. 2001). What was initially a qualitative description of the IR portion of the SED was quantified by Acke & van den Ancker (2004) where systems with $L_{\text{NIR}}/L_{\text{MIR}} \leq [12]-[60] + 0.9$ are Group I and the others are Group II. A different dividing line was proposed by van Boekel et al. (2005) where $L_{\text{NIR}}/L_{\text{MIR}} \leq [12]-[60] + 1.5$ are Group I sources. L_{NIR} is the integrated luminosity from 1 to $5 \mu\text{m}$, L_{MIR} is the integrated luminosity from $12-60 \mu\text{m}$, and $[12]-[60] = -2.5 \log(L_{12 \mu\text{m}}/L_{60 \mu\text{m}})$. $L_{12 \mu\text{m}}$ is the flux density at $12 \mu\text{m}$ and $L_{60 \mu\text{m}}$ is the flux density at $60 \mu\text{m}$.

Table 2
Stellar Parameters

Number	Star	Alt Name	SpT ^a	d^b pc	Group	$\log(T_{\text{eff}})^c$ K
1	HD 76534	OU Vel	B2	870 ^d	I	4.28
2	HD 259431	MWC 147	B5	170 ± 40	I	4.15
3	HD 250550	V1307 Ori	B7	1176 ± 1993	I	4.11
4	HD 100546	KR Mus	B9	97 ± 4	I	4.04
5	HD 31293	AB Aur	A0	140 ± 20	I	3.99
6	HD 179218	MWC 614	A0	250 ± 40	I	3.99
7	MWC 765	V380 Ori	A1	450 ^e	I	3.97
8	HD 36112	MWC 758	A8 ^f	280 ± 70	I	3.87
9	HD 135344b	SAO 206462	F4 ^g	140 ^g	I	3.83
10	LkH α 224	V1686 Cyg	F9/A4 ^h	980 ^o	I	3.92
11	HD 142527	...	F6 ⁱ	140 ± 20 ⁱ	I	3.82 ^j
12	HD 45677	FS Cma	B2	280 ± 70	II	4.33
13	HD 85567	V596 Car	B2 ^j	770 ^j	II	4.33
14	Elias 3-1	V892 Tau	B8.5-A0 ^k	140 ^k	I	4.02
15	HD 141569	...	B9.5	103 ± 8	II	4.01
16	HD 98922	...	B9/A2	1200 ± 500	II	3.95
17	HD 34282	V1366 Ori	A3 ^l	350 ^l	I	3.93
18	HD 190073	V1295 Aql	A2	767 ^m	II	3.95
19	HD 293782	UX Ori	A3	400 ^e	II	3.93
20	...	BF Ori	A5	450 ^e	II	3.91
21	...	CO Ori	F7	450 ⁿ	II	3.80
22	^p HD 37776	...	B2	330 ± 60
23	^p HD 196519	...	B8	241 ± 16
24	^p HD 172167	...	A0	7.7 ± 0.02
25	^p HD 102647	...	A3	11 ± 0.06
26	^p HD 13041	...	A4	58.7 ± 0.9
27	^p HD 11636	...	A5	18 ± 0.2
28	^p HD 28910	...	A8	49 ± 1
29	^p HD 8799	...	F4	25 ± 0.3

Notes.

^a The spectral types are adopted from Valenti et al. (2003) unless otherwise noted. These authors adopted the spectral type from either the Herbig & Bell 1988 or Th e et al. (1994) unless they found a large discrepancy between the UV spectrum of the star and the template spectrum. In such cases they adopted spectral type of the best fitting template.

^b From van Leeuwen (2007) unless otherwise noted.

^c Effective temperatures converted from the intrinsic $B - V$ color using the relationship described in Flower (1996) unless otherwise noted.

^d Herbst (1975).

^e Distance inferred by Blondel & Djie (2006) based on cluster membership.

^f Vieira et al. (2003).

^g Dunkin et al. (1997), Grady et al. (2009).

^h A4, Mora et al. (2001); F9, Hern andez et al. (2004).

ⁱ Mendigut a et al. (2014).

^j Hales et al. (2014).

^k Mooley et al. (2013).

^l Mer n et al. (2004).

^m Montesinos et al. (2009).

ⁿ Distance based on membership in 1 Ori, and cluster distance determined by Dolan & Mathieu (2001).

^o Distance inferred from membership in star forming region 2 Cyg and distance of 980 pc—Shevchenko et al. (1991).

^p Template stars used to estimate the UV luminosity of stars without IUE data.

The evolving definition of Group I and Group II has resulted in conflicting designations in the literature. For example, V380 Ori is labeled a Group II star by van Boekel et al. (2005) and Group I star by Fedele et al. (2011). Similarly, LkH α 224 is considered a Group II source by Acke et al. (2004) and a Group I source by Acke et al. (2010). Here we separate the sources into Group I and Group II using the IR photometry reported in Table 3 in order to self-consistently define our sample. We adopt the definition of Group I and Group II sources provided by van Boekel et al. (2005). The near-IR (NIR) flux was taken from 2MASS and WISE. The mid-IR (MIR) flux was taken from IRAS. To integrate the flux from the

photometric points, a 100 element array was created using cubic spline interpolation for both the measured specific flux and wavelength. The integral was determined numerically using the trapezoid rule.

The full sample is comprised of 13 Group I targets and 8 Group II targets (Figure 2). This sample includes several disks with large inner holes: HD 100546 (inferred from coronagraphic imagery; Grady et al. 2005), HD 135344b (inferred from SED modeling; Brown et al. 2007), HD 142527 (inferred from SED modeling combined with resolved MIR imagery; Verhoeff et al. 2011), HD 179218 (MIR interferometry; Menu et al. 2015), and HD 141569 (inferred from resolved MIR

Table 3
Circumstellar Data

No.	Star	[12]–[60]	$L_{\text{NIR}}/L_{\text{MIR}}$	L_{UV}^{a}	$L_{\text{UVS}}^{\text{b}}$	$L_{\text{UVL}}^{\text{c}}$	$L_{\text{PAH}}^{\text{d}}$	$L_{\text{PAH}}^{\text{d}}$	L_{CO}	L_{OH}
				L_{\odot}	L_{\odot}	L_{\odot}	$7.8 \mu\text{m}$	$11.3 \mu\text{m}$	(1, 0)P30	(1, 0)P4.5(+1, -1)
				$10^{-2} L_{\odot}$	$10^{-2} L_{\odot}$	$10^{-2} L_{\odot}$	$10^{-2} L_{\odot}$	$10^{-2} L_{\odot}$	$10^{-5} L_{\odot}$	$10^{-5} L_{\odot}$
1	HD 76534	6.08	2.13	1430 ^d	1043 ^d	166 ^d	$\leq 3.5^{\text{e}}$
2	HD 259431	2.35	1.10	15.1	10.4	3.5	...	2.86	$16 \pm 3^{\text{f}}$	$1.1 \pm 0.1^{\text{e}}$
3	HD 250550	0.51	1.75	157	93	48	≤ 25.7	≤ 3.86	$77 \pm 3^{\text{f}}$	$6.7 \pm 0.5^{\text{e}}$
4	HD 100546	1.00	0.34	8.5	5.9	2	9.31	11.3	$4.2 \pm 0.2^{\text{g}}$	$0.26 \pm 0.03^{\text{h}}$
5	HD 31293	1.47	2.49	7.8	4.2	3.3	10.8	0.66	$12.0 \pm 0.8^{\text{f}}$	$0.4 \pm 0.1^{\text{i}}$
6	HD 179218	0.27	1.01	21.7	13.5	6.8	28.4	2.78	$3.0 \pm 0.2^{\text{g}}$	$\leq 0.6^{\text{j}}$
7	MWC 765	2.36	1.30	8.6	5.7	3.1	21 ± 2	$4.9 \pm 0.7^{\text{e}}$
8	HD 36112	1.75	2.70	0.48 ^d	0.005 ^d	0.94 ^d	≤ 2.42	≤ 0.48	$12.3 \pm 1.4^{\text{g}}$	$0.9 \pm 0.2^{\text{i}}$
9	HD 135344b	3.02	3.45	0.05 ^d	0.001 ^d	0.19 ^d	0.85	0.16	1.3 ± 0.2	$\leq 0.3^{\text{j}}$
10	LkH α 224	2.23	0.46	1.8 ^d	0.6 ^d	1.20 ^d	≤ 71.7	≤ 2.08	...	$11.8 \pm 2.7^{\text{j}}$
11	HD 142527	2.51	1.87	2.8 ± 0.3	$0.1 \pm 0.1^{\text{k3}}$
12	HD 45677	-1.93	0.85	1430 ^d	1043 ^d	166 ^d	$\leq 2.4^{\text{e}}$
13	HD 85567	-1.65	6.78	1430 ^d	1043 ^d	166 ^d	42.6	7.17	...	$17.9 \pm 5.4^{\text{e}}$
14	Elias 3-1	0.85	0.29	8.3 ^d	5.1	2.6	7.47	1.52	...	$\leq 0.2^{\text{j}}$
15	HD 141569	2.51	10.7	8.3 ^d	5.1	2.6	0.38	0.03	$0.09 \pm 0.01^{\text{f}}$	$\leq 0.02^{\text{j}}$
16	HD 98922	-2.03	4.96	764	394	318	...	73.8	$172 \pm 9^{\text{g}}$	$\leq 47^{\text{e}}$
17	HD 34282	2.93	1.74	1.2	0.45	0.75	12.8	2.1	≤ 3	$\leq 0.8^{\text{e}}$
18	HD 190073	-1.43	6.72	35.6	15.8	25.8	≤ 5.47	≤ 3.65	$62.3 \pm 2^{\text{g}}$	$6.5 \pm 0.5^{\text{l}}$
19	UX Ori	0.07	2.63	0.51	0.23	0.32	≤ 1.15	≤ 0.36	2.2 ± 0.2	$\leq 1.5^{\text{e}}$
20	BF Ori	1.02	4.5	0.6	0.14	0.57	≤ 1.48	≤ 0.56	≤ 1.4	$\leq 0.6^{\text{e}}$
21	CO Ori	0.27	9.81	2.3	0.6	4.1	1.7 ± 0.9	$\leq 0.6^{\text{e}}$

Notes.

^a Integrated UV flux from 1300 to 2430 Å. From IUE spectra presented by Valenti et al. (2000, 2003) unless otherwise noted.

^b Integrated UV flux from 1300 to 1850 Å. From IUE spectra presented by Valenti et al. (2000, 2003) unless otherwise noted.

^c Integrated UV flux from 2430 to 3200 Å. From IUE spectra presented by Valenti et al. (2000, 2003) unless otherwise noted.

^d UV flux inferred from a template star with a matching spectral type from Valenti et al. (2003).

^e Fedele et al. (2011).

^f Brittain et al. (2007).

^g van der Plas et al. (2015).

^h Brittain et al. (2014).

ⁱ Mandell et al. (2008).

^j This work.

imagery; Marsh et al. 2002). HD 142527 has a low mass stellar companion orbiting near the inner rim of the circumstellar disk (Biller et al. 2012; Close et al. 2014).

The OH doublet is detected in 8 of the 13 Group I sources (61%) and 2 of the 8 Group II sources (25%). OH emission is observed in two of the five transition disk objects (HD 142527 and HD 100546). Several of the Group I sources for which OH is detected fall very close to the Group I/II boundary, and therefore the difference between the detection rate of OH emission from Group I and Group II HAeBes should be interpreted with caution. There is no clear trend between the luminosity of the OH emission and infrared colors of these stars (Figure 2).

We plot the luminosity of the $\nu = 1-0$ ${}^2\Pi_{3/2}$ P4.5 (1+, 1-) OH emission doublet relative to the $\nu = 1-0$ P30 CO line (Figure 3). The sources for which OH and CO are detected are well fit with a power law where $\log(L_{\text{OH}}) = (1.01 \pm 0.02)\log(L_{\text{CO}}) - (1.05 \pm 0.02)$. The typical ratio of the luminosity of the CO to the OH is 11.0 ± 0.2 . None of the non-detections of OH emission is sensitive enough to place an upper limit on the OH/CO ratio lower than the line fit to the detections. If the temperature and emitting area of the OH and CO gas are similar and the gas is optically thin, then the abundance of the OH gas is comparable to CO in systems spanning several dex in UV luminosity (see Table 3). The

transition disks are clustered among the weakest OH and CO emitters in the sample (Figures 3, 5, and 6).

For five of the sources in our sample, we have resolved OH and CO emission lines. The line profiles of the OH and CO emission lines are consistent to within the signal to noise for four of the stars (though the signal-to-noise ratio (S/N) of HD 142527 is too low to say anything definitive; Figure 4). The exception is HD 100546 where the OH and CO line profiles are not consistent (see also Liskowsky et al. 2012). While the widths of the HD 100546 lines are similar, the shapes of the asymmetries are different. Previous studies of the CO emission show that the the $\nu = 1-0$ lines are comprised of two components—a symmetric line arising from the circumstellar disk extending from ~ 14 au to beyond 50 au and a variable component arising from a localized source of emission in a Keplerian orbit near the inner edge of the circumstellar disk (Brittain et al. 2014).

To explore the role the stellar UV field plays in producing the observed molecular emission, we compare the luminosity of the OH, CO, and PAH emission to the ultraviolet luminosity of the HAeBes (Figures 5–7). Most of the sources were observed with IUE (Table 3; Valenti et al. 2000, 2003). For sources not observed with IUE, we determined the spectral type of the star and calculated the UV luminosity from a matching stellar template (see Table 3 for the template stars). One star, HD 142527 (SpT F6), has no template or UV observation and

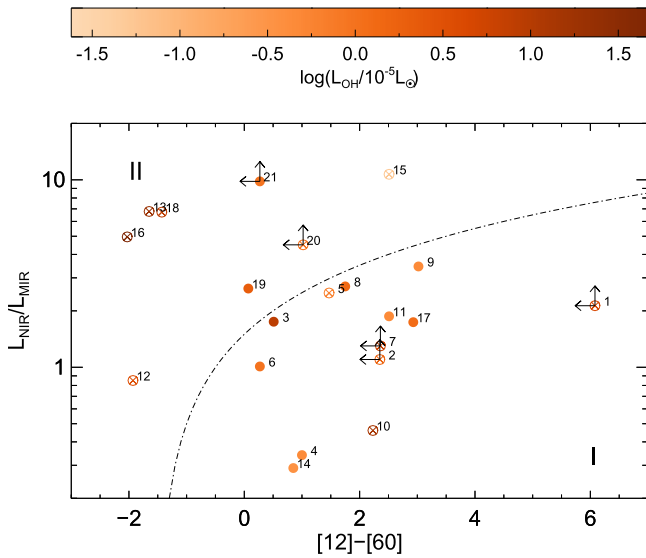


Figure 2. Group selection of sources. Herbig Ae/Be stars are separated into two groups on the basis of their IR colors. Group I sources have $L_{\text{NIR}}/L_{\text{IR}} \leq [12]-[60] + 1.5$ (e.g., van Boekel et al. 2005). The dotted-dashed line separates the Group I and Group II sources. The filled sources are sources for which OH was detected and the open circles are non-detections. The logarithm of the luminosity of the observed line or its upper limit is indicated by the color scale. Several of our targets fall near the Group I/Group II boundary. There is no apparent trend between the luminosity of the OH emission and the group classification.

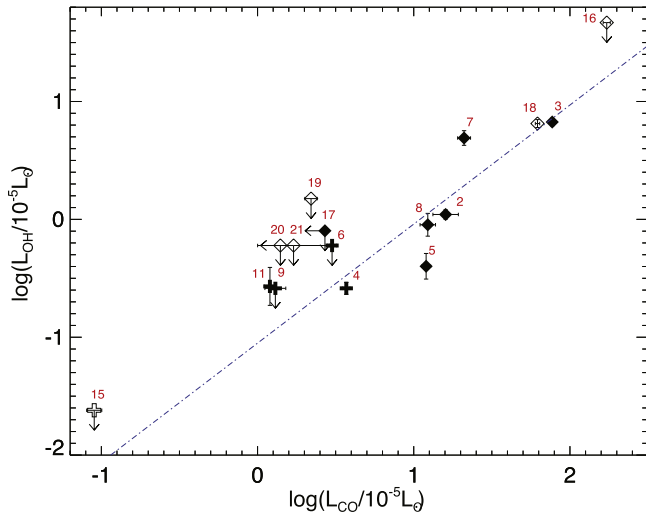


Figure 3. Logarithm of the luminosity of the $\nu = 1-0 \text{ } ^2\Pi_{3/2} \text{ P4.5 (1+, 1-)} \text{ OH}$ doublet is plotted vs. the logarithm of the $\nu = 1-0 \text{ P30 CO}$ line. Group I Herbig Ae/Be stars are marked with filled points. Group II Herbig Ae/Be stars are marked with open symbols. The disks for which holes have been identified are indicated with “plus” signs, while those without holes are indicated with diamonds. A linear least-squares fit to the detections is plotted with a blue dotted-dashed line. None of the upper limits on the non-detection of OH emission falls below this trend. OH emission is only detected in two transition disk sources, HD 142527 and HD 100546. The luminosity of OH emission tends to be weaker for transitional disks compared to disks without inner holes.

is left out of this analysis. Stars with a spectral type later than A5 may have a UV flux dominated by the accretion luminosity of the star, thus the UV luminosity reported for these objects should be taken as a lower limit. We consider the short-wavelength portion of the UV spectrum ($1300 \text{ \AA} \leq \lambda \leq 1850 \text{ \AA}$; L_{UVS}) separately from the long-wavelength portion

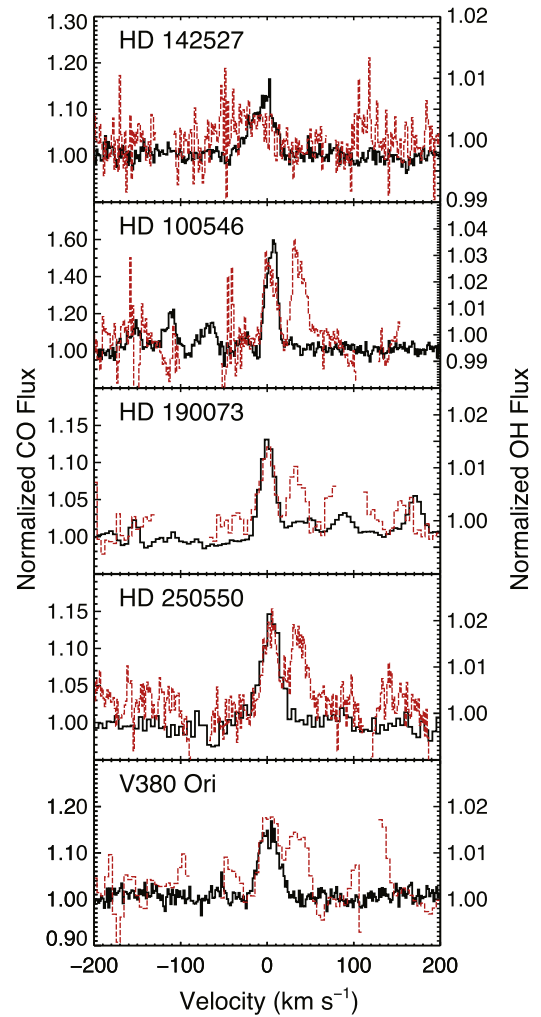


Figure 4. Comparison of a high- $J \nu = 1-0 \text{ CO}$ line with the $\nu = 1-0 \text{ P4.5(1+, -1) OH}$ doublet. For HD 100546, and V380 Ori, the $\nu = 1-0 \text{ P26 CO}$ line is compared with the $\nu = 1-0 \text{ P4.5(1+) OH}$ line. For HD 190073 and HD 250550 the $\nu = 1-0 \text{ P30 CO}$ line is compared with the $\nu = 1-0 \text{ P4.5(1+) OH}$ line. For HD 142527 the $\nu = 1-0 \text{ P26 CO}$ line is compared to the $\nu = 1-0 \text{ P4.5(-1) OH}$ line. In each panel, the CO spectrum is plotted with a black line, the OH spectrum is plotted with a red dashed line. There is no significant difference between the line profile of the OH and CO lines for HD 190073, HD 250550, or V380 Ori. In the case of HD 100546, the shape of the lines are different (see Liskowsky et al. 2012). The S/N of the OH line profile for HD142527 is too low to say anything definitive.

($2430 \text{ \AA} \leq \lambda \leq 3200 \text{ \AA}$; L_{UVL}). The radiation at the short-wavelength end of the spectrum enhances OH emission both by photodissociating H_2O to produce OH, possibly in an excited state, and by heating the gas. The longer-wavelength radiation excites PAHs.

In Figure 5, we plot the luminosity of the OH doublet as a function of the short-wavelength ultraviolet luminosity. The sources that are brightest at UV wavelengths also reveal the brightest OH emission lines. The stars with transition disks have weaker OH emission than HAeBes of the same L_{UVS} . To quantify the correlation between the logarithm of the OH luminosity and the logarithm of the short wavelength luminosity we apply Kendall’s τ correlation test using ASURV Rev 1.2 (Isobe et al. 1990; Lavalley et al. 1992), which implements the methods presented in Isobe et al. (1986). This test finds that there is a 1.5% chance that a correlation is not present in the data. We use the Buckley–James

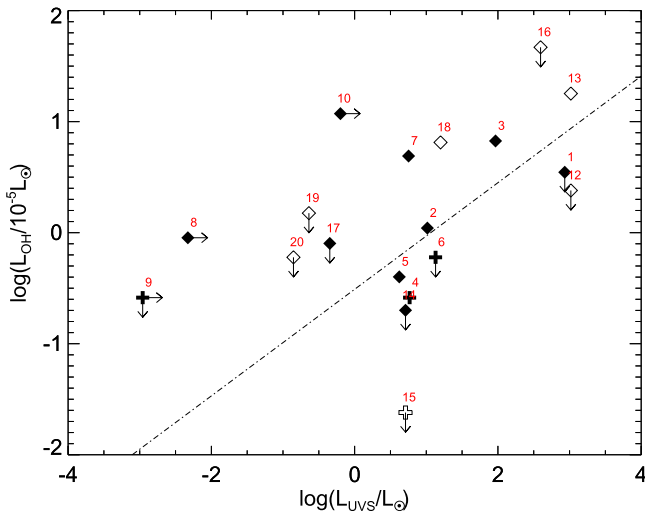


Figure 5. Logarithm of the luminosity of the $\nu = 1-0$ $^2\Pi_{3/2}$ P4.5 (1+, 1-) OH doublet is plotted vs. the logarithm of the ultraviolet luminosity integrated from 1300 to 1850 Å (L_{UVS}). The same symbols are repeated from Figure 3. Several of the stars do not have direct UV flux measurements. The UV luminosity of these stars was inferred from main-sequence template stars. The accretion luminosity of stars with a spectral-type later than A5 may provide a significant fraction of the flux that is unaccounted for by this measurement, thus they are noted as lower limits. The transition disks in the sample are systematically offset from the broader sample. The result of the Buckley–James regression is plotted with the dotted–dashed line $0.48 \log(L_{UVS}/L_{\odot}) - 0.51$.

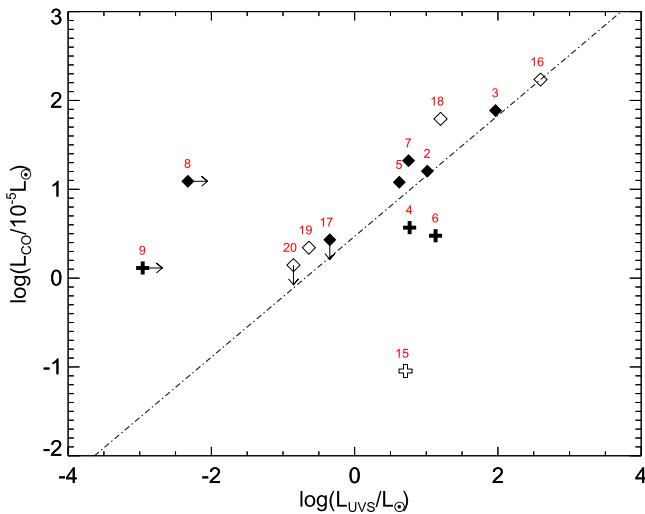


Figure 6. Logarithm of the luminosity of the $\nu = 1-0$ P30 CO line is plotted vs. the logarithm of the ultraviolet luminosity integrated from 1300 to 1850 Å (L_{UVS}). The same symbols are repeated from Figure 3. The transition disks in the sample are systematically offset from the broader sample. The result of the Buckley–James regression is plotted with the dotted–dashed line $0.68 \log(L_{UVS}/L_{\odot}) + 0.47$.

regression test using ASURV Rev 1.2 to find the best least-squares fit to the data and find $\log(L_{OH}/10^{-5} L_{\odot}) = (0.45 \pm 0.25) \log(L_{UVS}/L_{\odot}) - 0.93$.

One outlier in this data set is the transition disk HD 141569 (source 15). HD 141569 is a low-mass transition disk with a large inner hole and cool molecular gas (e.g., Zuckerman et al. 1995; Brittain et al. 2003; Dent et al. 2005). This source has a particularly low gas (Thi et al. 2014) and dust mass (Dent et al. 2005) and bridges the gap between gas rich transition disks and debris disks mostly emptied of their primordial gas. If the OH and CO in the system are roughly the same temperature

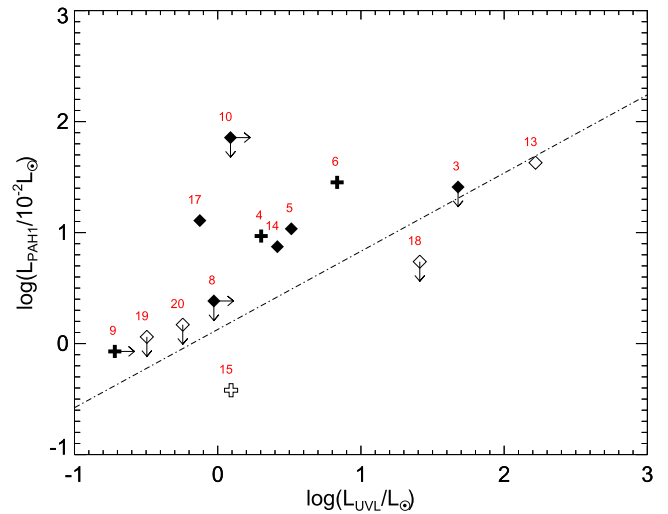


Figure 7. Logarithm of the luminosity of the 7.8 μm PAH line is plotted vs. the logarithm of the ultraviolet luminosity integrated from 2430 to 3200 Å (L_{UVL}). The same symbols are repeated from Figure 3. The transition disks in the sample are not systematically offset from the broader sample. The result of the Buckley–James regression is plotted with the dotted–dashed line $0.37 \log(L_{UVL}/L_{\odot}) + 0.61$.

(~ 200 K; Brittain et al. 2007), it is unlikely that the upper states of the $\nu = 1-0$ $^2\Pi_{3/2}$ P4.5 (1+, 1-) OH doublet will be populated at the same level as the other systems with much warmer gas. Unfortunately, the lower-J OH lines are generally not accessible from the ground except under exceptionally dry conditions. If we set aside HD 141569 from our statistical analysis, the probability that the data are not correlated does not change substantially (1%), and the fit to the data from the Buckley–James method changes to $\log(L_{OH}/10^{-5} L_{\odot}) = (0.48 \pm 0.24) \log(L_{UVS}/L_{\odot}) - 0.51$.

In Figure 6, we plot the the luminosity of the CO emission as a function of the short wavelength ultraviolet luminosity and see a similar trend. The stars with transition disks also show systematically lower CO emission than their classical counterparts with comparable L_{UVS} . The correlation test by the generalized Kendall’s τ indicates that the probability that the data are not correlated is 0.07% if we set aside HD 141569. The linear regression using the Buckley–James method indicates that $\log(L_{CO}/10^{-5} L_{\odot}) = (0.68 \pm 0.17) \log(L_{UVS}/L_{\odot}) + 0.47$.

Finally, we consider the relationship between the log of the luminosity of the PAHs and the log of the UV luminosity (Figure 7). While the trend is similar, there is more scatter and the transition disk objects are not systematically fainter than the other sources. However, the luminosities of the PAH emission from the Group II sources is lower than those from the Group I sources with the same long-wavelength UV luminosity. The probability that the quantities are not correlated is 5% and the linear regression by the Buckley–James method indicates that $\log(L_{PAH}/10^{-2} L_{\odot}) = (0.37 \pm 0.12) \log(L_{UVL}/L_{\odot}) + 0.61$.

4. DISCUSSION AND CONCLUSIONS

The disks surrounding HAeBes are gas rich as evidenced by their high accretion rates (Fairlamb et al. 2015; Mendigutía et al. 2015). However, HAeBes are powerful UV emitters, making protoplanetary disks challenging environments for the synthesis and survival of prebiotic molecules, particularly when grains, the usual UV absorbers, have settled out of disk atmospheres. Recent studies of T Tauri disks, the lower mass

counterparts of HAeBes, show how water synthesized in disk atmospheres absorbs stellar UV through photodissociation, yielding OH (Bethell & Bergin 2009; Ádámkóvics et al. 2014; Du & Bergin 2014).

The trends observed in Figures 3, 5, 6, and 7 can be explained simply in this picture of a disk irradiated by stellar UV photons. In dissociating water at the disk surface, the UV not only enhances the abundance of OH there, but it also heats the disk surface (Ádámkóvics et al. 2014, 2016; Du & Bergin 2014; Glassgold & Najita 2015).

In models of UV-irradiated disk atmospheres (e.g., Ádámkóvics et al. 2016), CO and OH are both abundant in the warm surface region of the disk atmosphere (at ~ 1000 K), which is heated by UVS (FUV continuum and Ly α) through photodissociation and photochemical pathways. In accordance with this picture, we find that the CO and OH line profiles are consistent with each other (Figure 4), hinting that the gas arises from the same region of the disk, as expected from models.

The excitation mechanism of the OH emission discussed here is uncertain. In principle, OH can be UV fluoresced similarly to CO as OH possesses bound excited electronic states. However, collisions can quench UV fluorescence such that the final population of the vibrational levels of OH are determined collisionally. When collisional cross sections for vibrational excitation of OH with partner species such as H, H₂, and He are available, detailed studies of OH excitation can be carried out. In the meantime, our data hint that the OH and CO excitation mechanism are related, as the ratio of their fluxes are constant over a wide range of disk geometries and UV luminosities (Figure 3).

Group I disks are flared while Group II disks are flat (Meeus et al. 2001), thus Group I disks intercept a larger fraction of the stellar flux. Because of this, one might expect that the ro-vibrational emission of molecules would be brighter among Group I disks than among Group II disks. This difference is not observed (Figure 2), nor do we find a difference in the relationship between OH and the UV luminosity or CO and the UV luminosity between Group I HAeBes and Group II HAeBes. One possibility is that this grouping conflates varying degrees of disk clearing and flaring (e.g., Menu et al. 2015) obscuring any distinction in luminosity of ro-vibrational emission lines between Group I and Group II sources.

We have identified five systems in our sample with cleared inner disks. Compared to the “normal” HAeBes, transition disks are missing the warm disk close to the star, so they are expected to have systematically fainter OH and CO emission relative to full disks (Figures 3, 5, and 6). In contrast to the CO and OH emission, which depends on the intensity of incident UVS photons, PAH emission can be generated by UVL photons that are absorbed at any distance from the star. As long as the disk intercepts the long-wavelength ultraviolet radiation at some radius, PAH emission can be produced. As a result, PAH emission should depend less sensitively on whether the inner disk is missing or not. Accordingly, the transition disk objects are not systematically offset relative to the full disks (Figure 7). However, the amount of disk flaring will affect the PAH luminosity. As a result, the less flared Group II sources have systematically fainter PAH flux for the same long-wavelength UV luminosity.

Further work can better quantify the relation of ro-vibrational OH emission to ro-vibrational CO emission. We did not measure the rotational temperature of the OH for the stars in

our sample, nor do we have the data necessary to explore the excitation mechanism of the OH. For most of the sources where OH is detected, only the P4.5 doublet was targeted. In a few sources where there was a detection of OH, there are no corresponding CO observations. If the OH and CO are co-radially located but at different temperatures, this will suggest that we are probing gas at different depths into the disk. The data do not show evidence of enhanced OH emission concentrated at the inner rim of disks with holes; however, higher resolution and signal to noise data of the transition disk objects are necessary to draw firm conclusions. The availability of new large-format detectors on high-resolution NIR spectrographs such as iSHELL on NASA’s Infrared Telescope Facility and the refurbished CRIRES on ESO’s VLT will enable such studies.

Some of the data presented herein were obtained at the W.M. Keck Observatory, which is operated as a scientific partnership among the California Institute of Technology, the University of California and the National Aeronautics and Space Administration. The Observatory was made possible by the generous financial support of the W.M. Keck Foundation. The authors wish to recognize and acknowledge the very significant cultural role and reverence that the summit of Mauna Kea has always had within the indigenous Hawaiian community. We are most fortunate to have the opportunity to conduct observations from this mountain. This research has also made use of the Keck Observatory Archive, which is operated by the W. M. Keck Observatory and the NASA Exoplanet Science Institute, under contract with the National Aeronautics and Space Administration. Based also in part on data obtained from the ESO Science Archive Facility. Based also in part on observations obtained at the Gemini Observatory (GS-2005B-C-2) which is operated by the Association of Universities for Research in Astronomy, Inc., under a cooperative agreement with the NSF on behalf of the Gemini partnership: the National Science Foundation (United States), the National Research Council (Canada), CONICYT (Chile), Ministerio de Ciencia, Tecnología e Innovación Productiva (Argentina), and Ministério da Ciência, Tecnologia e Inovação (Brazil). This paper is based in part on observations obtained with the Phoenix infrared spectrograph, developed and operated by the National Optical Astronomy Observatory. S.D.B. acknowledges support for this work from the National Science Foundation under grant number AST-0954811. Basic research in infrared astronomy at the Naval Research Laboratory is supported by 6.1 base funding.

Facilities: Keck (NIRSPEC), Very Large Telescope:UT1 (CRIRES), Gemini South (PHOENIX).

REFERENCES

- Acke, B., Bouwman, J., Juhász, A., et al. 2010, *ApJ*, 718, 558
 Acke, B., & van den Ancker, M. E. 2004, *A&A*, 426, 151
 Acke, B., van den Ancker, M. E., Dullemond, C. P., van Boekel, R., & Waters, L. B. F. M. 2004, *A&A*, 422, 621
 Ádámkóvics, M., Glassgold, A. E., & Najita, J. R. 2014, *ApJ*, 786, 135
 Ádámkóvics, M., Najita, J. R., & Glassgold, A. E. 2016, *ApJ*, 817, 82
 Banzatti, A., & Pontoppidan, K. M. 2015, *ApJ*, 809, 167
 Bethell, T., & Bergin, E. 2009, *Sci*, 326, 1675
 Biller, B., Lacour, S., Juhász, A., et al. 2012, *ApJL*, 753, L38
 Blake, G. A., & Boogert, A. C. A. 2004, *ApJL*, 606, L73
 Blondel, P. F. C., & Djie, H. R. E. T. A. 2006, *A&A*, 456, 1045
 Brittain, S. D., Carr, J. S., Najita, J. R., Quanz, S. P., & Meyer, M. R. 2014, *ApJ*, 791, 136
 Brittain, S. D., Rettig, T. W., Simon, T., et al. 2003, *ApJ*, 588, 535

- Brittain, S. D., Simon, T., Najita, J. R., & Rettig, T. W. 2007, *ApJ*, **659**, 685
- Brown, J. M., Blake, G. A., Dullemond, C. P., et al. 2007, *ApJL*, **664**, L107
- Close, L. M., Follette, K. B., Males, J. R., et al. 2014, *ApJL*, **781**, L30
- Dent, W. R. F., Greaves, J. S., & Coulson, I. M. 2005, *MNRAS*, **359**, 663
- Dolan, C. J., & Mathieu, R. D. 2001, *AJ*, **121**, 2124
- Du, F., & Bergin, E. A. 2014, *ApJ*, **792**, 2
- Dullemond, C. P., & Monnier, J. D. 2010, *ARA&A*, **48**, 205
- Dunkin, S. K., Barlow, M. J., & Ryan, S. G. 1997, *MNRAS*, **286**, 604
- Fairlamb, J. R., Oudmaijer, R. D., Mendigutía, I., Ilee, J. D., & van den Ancker, M. E. 2015, *MNRAS*, **453**, 976
- Fedele, D., Pascucci, I., Brittain, S., et al. 2011, *ApJ*, **732**, 106
- Flower, P. J. 1996, *ApJ*, **469**, 355
- Glassgold, A. E., & Najita, J. R. 2015, *ApJ*, **810**, 125
- Grady, C. A., Schneider, G., Sitko, M. L., et al. 2009, *ApJ*, **699**, 1822
- Grady, C. A., Woodgate, B., Heap, S. R., et al. 2005, *ApJ*, **620**, 470
- Hales, A. S., De Gregorio-Monsalvo, I., Montesinos, B., et al. 2014, *AJ*, **148**, 47
- Herbig, G. H. 1960, *ApJS*, **4**, 337
- Herbig, G. H., & Bell, K. R. 1988, Third Catalog of Emission-Line Stars of the Orion Population, Vol. 3 (Heidelberg: Astronomisches Rechen-Institut)
- Herbst, W. 1975, *AJ*, **80**, 212
- Hernández, J., Calvet, N., Briceño, C., Hartmann, L., & Berlind, P. 2004, *AJ*, **127**, 1682
- Hinkle, K. H., Blum, R. D., Joyce, R. R., et al. 2003, *Proc. SPIE*, **4834**, 353
- Hinkle, K. H., Cuberly, R. W., Gaughan, N. A., et al. 1998, *Proc. SPIE*, **3354**, 810
- Hinkle, K. H., Joyce, R. R., Sharp, N., & Valenti, J. A. 2000, *Proc. SPIE*, **4008**, 720
- Honda, M., Maaskant, K., Okamoto, Y. K., et al. 2012, *ApJ*, **752**, 143
- Isobe, T., Feigelson, E. D., Akritas, M. G., & Babu, G. J. 1990, *ApJ*, **364**, 104
- Isobe, T., Feigelson, E. D., & Nelson, P. I. 1986, *ApJ*, **306**, 490
- Johnson, J. A., Howard, A. W., Bowler, B. P., et al. 2010, *PASP*, **122**, 701
- Käufel, H.-U., Ballester, P., Biereichel, P., et al. 2004, *Proc. SPIE*, **5492**, 1218
- Kunde, V. R., & Maguire, W. C. 1974, *QJRT*, **14**, 803
- Lagrange, A.-M., Gratadour, D., Chauvin, G., et al. 2009, *A&A*, **493**, L21
- Lavalley, M., Isobe, T., & Feigelson, E. 1992, in ASP Conf. Ser. 25, Astronomical Data Analysis Software and Systems I, ed. D. M. Worrall, C. Biemesderfer, & J. Barnes (San Francisco, CA: ASP), 245
- Liskowsky, J. P., Brittain, S. D., Najita, J. R., et al. 2012, *ApJ*, **760**, 153
- Maaskant, K. M., Honda, M., Waters, L. B. F. M., et al. 2013, *A&A*, **555**, A64
- Mandell, A. M., Mumma, M. J., Blake, G. A., et al. 2008, *ApJL*, **681**, L25
- Marsh, K. A., Silverstone, M. D., Becklin, E. E., et al. 2002, *ApJ*, **573**, 425
- McLean, I. S., Becklin, E. E., Bendiksen, O., et al. 1998, *Proc. SPIE*, **3354**, 566
- Meeus, G., Waters, L. B. F. M., Bouwman, J., et al. 2001, *A&A*, **365**, 476
- Mendigutía, I., de Wit, W. J., Oudmaijer, R. D., et al. 2015, *MNRAS*, **453**, 2126
- Mendigutía, I., Fairlamb, J., Montesinos, B., et al. 2014, *ApJ*, **790**, 21
- Menu, J., van Boekel, R., Henning, T., et al. 2015, *A&A*, **581**, A107
- Merín, B., Montesinos, B., Eiroa, C., et al. 2004, *A&A*, **419**, 301
- Montesinos, B., Eiroa, C., Mora, A., & Merín, B. 2009, *A&A*, **495**, 901
- Mooley, K., Hillenbrand, L., Rebull, L., Padgett, D., & Knapp, G. 2013, *ApJ*, **771**, 110
- Mora, A., Merín, B., Solano, E., et al. 2001, *A&A*, **378**, 116
- Rothman, L. S., Barbe, A., Benner, D. C., et al. 2003, *QJRT*, **82**, 5
- Shevchenko, V. S., Ibragimov, M. A., & Chernysheva, T. L. 1991, *AZh*, **68**, 466
- Su, K. Y. L., Rieke, G. H., Misselt, K. A., et al. 2005, *ApJ*, **628**, 487
- Su, K. Y. L., Rieke, G. H., Stansberry, J. A., et al. 2006, *ApJ*, **653**, 675
- The, P. S., de Winter, D., Perez, M. R., & The, P. S. 1994, *A&AS*, **104**, 315
- Thi, W.-F., Pinte, C., Pantin, E., et al. 2014, *A&A*, **561**, A50
- Valenti, J. A., Fallon, A. A., & Johns-Krull, C. M. 2003, *ApJS*, **147**, 305
- Valenti, J. A., Johns-Krull, C. M., & Linsky, J. L. 2000, *ApJS*, **129**, 399
- van Boekel, R., Min, M., Waters, L. B. F. M., et al. 2005, *A&A*, **437**, 189
- van der Plas, G., van den Ancker, M. E., Waters, L. B. F. M., & Dominik, C. 2015, *A&A*, **574**, A75
- van Leeuwen, F. 2007, *A&A*, **474**, 653
- Verhoeff, A. P., Min, M., Pantin, E., et al. 2011, *A&A*, **528**, A91
- Vieira, S. L. A., Corradi, W. J. B., Alencar, S. H. P., et al. 2003, *AJ*, **126**, 2971
- Waters, L. B. F. M., & Waelkens, C. 1998, *ARA&A*, **36**, 233
- Zuckerman, B., Forveille, T., & Kastner, J. H. 1995, *Natur*, **373**, 494
- Zuckerman, B., Melis, C., Klein, B., Koester, D., & Jura, M. 2010, *ApJ*, **722**, 725